Ultrasound in Med. & Biol., Vol. 34, No. 2, pp. 276–288, 2008

0301-5629/08/$–see front matter

ELSEVIER

doi:10.1016/j.ultrasmedbio.2007.07.011

● *Original Contribution*

TWO-DIMENSIONAL SONOELASTOGRAPHIC SHEAR VELOCITY IMAGING

KENNETH HOYT, BENJAMIN CASTANEDA, and KEVIN J. PARKER
Department of Electrical and Computer Engineering and the Rochester Center for Biomedical Ultrasound, University of Rochester, Rochester, NY, USA

(*Received* 19 *January* 2007, *revised* 25 *June* 2007, *in final form* 19 *July* 2007)

Abstract—We introduce a novel 2-D sonoelastographic technique for estimating local shear velocities from propagating shear wave interference patterns (termed crawling waves) in this paper. A relationship between the local crawling wave spatial phase derivatives and local shear wave velocity is derived, with phase derivatives estimated using a 2-D autocorrelation technique. Comparisons were made between the 2-D sonoelastographic shear velocity estimation technique and its computationally simpler 1-D precursor. In general, the 2-D sonoelastographic shear velocity estimator outperformed the 1-D–based technique in terms of accuracy and estimator noise minimization. For both approaches, increasing the estimator kernel size reduces noise levels but lowers spatial resolution. Homogeneous elastic phantom results demonstrate the ability of sonoelastographic shear velocity imaging to quantify the true underlying shear velocity distributions as verified using time-of-flight measurements. Results also indicate that increasing the estimator kernel size increases the transition zone length about boundaries in heterogeneous elastic mediums and may complicate accurate quantification of smaller elastically contrasting lesions. Furthermore, analysis of contrast-to-noise ratio (CNR) values for sonoelastograms obtained in heterogeneous elastic phantoms reveal that the 2-D sonoelastographic shear velocity estimation technique outperforms the 1-D version for a given kernel size in terms of image noise minimization and contrast enhancement. Experimental results from an embedded porcine liver specimen with a radiofrequency ablation (RFA) lesion demonstrates that the 2-D sonoelastographic shear velocity estimation technique minimizes image noise artifacts and yields a consistent lesion boundary when compared with gross pathology. Volume measurements of the RFA lesion obtained from shear velocity sonoelastograms was comparable to that obtained by fluid displacement of the dissected lesion as illustrated by 3-D volume reconstructions. Overall, 2-D sonoelastographic shear velocity imaging was shown to be a promising new approach to characterizing the shear velocity distribution of elastic materials. (E-mail: hoyt@ece.rochester.edu)

Key Words: **Crawling waves, Elasticity imaging, Shear velocity estimation, Shear wave interference patterns, Sonoelastography.**

INTRODUCTION

Palpation is a routine physical examination whereby physicians qualitatively assess the elastic properties of soft tissue. During palpation, stiff masses that are discrete and differ from the surrounding tissue are considered suspicious for malignancy. Although these discrete masses may dislocate or feel fixed within the tissue, subtle findings are much more difficult to interpret. Specifically, in many tumor cases, despite the difference in stiffness, the small size of a pathological lesion or its deep location impedes detection and evaluation by palpation. In addition, lesions may or may not exhibit physical properties that allow detection using conventional medical imaging modalities such as computed tomography, magnetic resonance or ultrasound.

For more than two decades, the development of ultrasound-based imaging techniques for depicting the elastic properties of biological tissues has been the focal point of an international research endeavor (Gao et al. 1996; Ophir et al. 1999; Greenleaf et al. 2003). The universal goal of these initiatives revolves around mapping some tissue mechanical property in an anatomically meaningful manner to describe valuable clinical information. Because changes in tissue stiffness are typically indicative of an abnormal pathological process (Anderson and Kissane 1977), imaging parameters related to tissue elasticity may finally provide a reliable gateway for differentiating normal from abnormal tissues.

Vibrational sonoelastography is a tissue elasticity imaging technique that estimates the amplitude response

Address correspondence to: Dr. Kenneth Hoyt, Department of Electrical and Computer Engineering, University of Rochester, 204 Hopeman Building, Rochester, NY 14627 USA. E-mail: hoyt@ece.rochester.edu

of tissues under harmonic mechanical excitation using ultrasonic Doppler techniques (Lerner et al. 1988). Because of a mathematical relationship between particle vibrational response and received Doppler spectral variance (Huang et al. 1990), low-frequency (50–500 Hz) and low-amplitude (20–100 μm) shear waves propagating in tissue can be visualized using sonoelastography to detect regions of abnormal stiffness (Parker et al. 1998).

Recently, it was shown that interfering shear waves produce slowly propagating interference patterns with an apparent velocity much less than (but proportional to) the underlying true shear velocity (Wu et al. 2004). Termed crawling waves, they are generated using a pair of mechanical sources vibrating at slightly offset frequencies or by continuously phase shifting one of the source excitation signals. The resultant shear wave interference patterns can be visualized in real-time using sonoelastographic imaging techniques. In general, crawling wave images describe shear wave propagation patterns and allow local estimation of shear velocity distributions (Wu et al. 2006; McLaughlin et al. 2006; Hoyt et al. 2006). Assuming that the local shear velocity values are proportional to the square root of the shear modulus, spatial mapping of either parameter allows production of quantitative tissue elasticity images.

A real-time sonoelastographic technique for estimating local shear velocities from crawling wave images was introduced by Hoyt et al. (2006). Specifically, a relationship between crawling wave phase derivatives and local shear wave velocity was derived, with phase derivatives estimated using an autocorrelation-based technique. However, this method computes local shear velocities using a 1-D kernel and estimator and is conducted independent of shear wave displacement data in neighboring depth regions. Despite promising initial results using this shear velocity imaging technique, a more accurate and robust estimator may be realized by utilizing a 2-D shear velocity estimation algorithm. In this paper, a 2-D sonoelastographic shear velocity imaging technique is introduced. Performance of this novel tissue elasticity imaging modality is compared in simulation and experiments to results obtained using its 1-D precursor, followed by a conclusion.

THEORY

Elastic properties of soft tissue

We begin by considering the wave motion equation for a linear and isotropic medium in terms of the displacements as:

$$\frac{E}{2(1+\nu)}\nabla^2\bar{u} + \frac{E}{2(1+\nu)(1-2\nu)}\nabla\,\nabla\cdot\bar{u} = \rho\frac{\partial^2\bar{u}}{\partial t^2}, \quad (1)$$

where E, ν, ρ, $\bar{u}$ and t are the Young's modulus, Poisson's ratio, mass density, displacement vector and time variable, respectively. As described by Landau and Lifshitz (1986), eqn (1) can be decomposed into two decoupled motion equations: one governing longitudinal wave motion and the other governing shear wave motion. In a homogeneous medium, the shear wave component is described by the following wave equation:

$$\nabla^2\bar{u}_s - \frac{1}{v_s^2}\frac{\partial^2\bar{u}_s}{\partial t^2} = 0, \quad (2)$$

where $\bar{u}_s$ is the shear displacement vector and v_s denotes the shear wave velocity expressed as:

$$v_s = \sqrt{\frac{E}{2\rho(1+\nu)}}. \quad (3)$$

Furthermore, if we consider propagating shear waves in soft tissue (*i.e.*, a nearly incompressible medium) then eqn (3) can be further simplified to:

$$v_s = \sqrt{\frac{E}{3\rho}} = \sqrt{\frac{G}{\rho}}, \quad (4)$$

which relates the shear wave velocity to the shear modulus G and mass density of a homogeneous tissue sample.

Sonoelastographic imaging

In conventional sonoelastographic imaging, low-frequency mechanical vibrations are used to noninvasively excite shear waves in tissue. Given the tissue vibrational response from propagating shear waves, elasticity information can be estimated in depth using ultrasonic Doppler techniques. The Doppler shift of an ultrasonic wave scattered from a spatially oscillating object (tissue volume) is given by a Fourier-Bessel series of equally spaced harmonics above and below the Doppler carrier frequency (Huang et al. 1990). It has been demonstrated that the vibrational amplitude of tissue scatterers in sinusoidal motion predictably alters the power spectrum of an insonifying ultrasound beam. Specifically, a linear relationship exists between the vibrational amplitude and standard deviation of the backscattered power spectrum (Huang et al. 1990) and constitutes the governing principle behind sonoelastographic imaging. A modified pulsed Doppler ultrasound system allows imaging in real-time to reflect changes in deep-tissue stiffness (Parker et al. 1998). In practice, when a region of tissue contains a stiff focal lesion or mass, a local decrease in peak vibrational amplitude results. See Taylor et al. (2000) for a description of the Doppler signal processing techniques utilized in real-time sonoelastographic imaging.

Moving shear wave interference patterns

As introduced by Wu et al. (2004), shear wave interference patterns can be generated by two coherent monochromatic vibration sources and imaged using sonoelastography. Moreover, if the two sources vibrate at slightly offset frequencies f_s and $f_s + \Delta f_s$, respectively, then the interference patterns move at an apparent velocity equal to $\Delta f_s/2f_s \cdot v_s$. These moving shear wave interference patterns have been termed crawling waves. In practice, the frequency difference Δf_s is normally chosen to be in the range of $f_s/100$ to $f_s/250$. Using a higher frequency offset can introduce a beat frequency that may compromise imaging results. Owing to the properties of these interfering shear waves, the spacing between the pattern bands equals half of the shear wavelength. Hence, analysis of the local shear wave interference patterns (or crawling wave image frame) allows estimation of the governing shear velocity distribution.

One-dimensional shear velocity estimation

As shown by Hoyt et al. (2006), shear wave interference displacement fields $u(m, n)$, excited using a pair of monochromatic mechanical sources, can be expressed as standing wave patterns:

$$u(m,n) = 2A^2\exp(-\alpha D)\left[\cosh(2\alpha n T_n) + \cos(2k_s n T_n + \Delta k_s n T_n)\right], \quad (5)$$

where m and n are integer values denoting row and column matrix indices (*i.e.*, spatial coordinates), respectively, A is the excitation source amplitude, α is the shear wave attenuation coefficient, D is the excitation source separation distance, T_n denotes the spatial sampling interval along the n-axis (*i.e.*, shear wave propagation axis or lateral direction) and k_s and Δk_s denote the shear wave number and difference, respectively. Note that eqn (5) assumes that the shear wave displacement data is parallel to a line of sight connecting the vibration sources. Moreover, eqn (5) assumes plane wave conditions and can be realized in practice by imaging in the far field of the shear wave sources (Wu et al. 2006). For discrete shear wave displacement data, the analytic signal $\hat{u}(m, n)$ of $u(m, n)$ is defined as:

$$\hat{u}(m,n) = u(m,n) - j\breve{u}(m,n), \quad (6)$$

where $\breve{u}(m, n)$ denotes the discrete 1-D Hilbert transform of $u(m, n)$ along the n-axis:

$$\breve{u}(m,n) = \frac{-1}{\pi n}u(m,n). \quad (7)$$

The shear velocity in 1-D space can be estimated by evaluating the phase of the 1-D autocorrelation function $\hat{\gamma}(n')$ of the analytic signal $\hat{u}(m, n)$:

$$\hat{\gamma}(n') = \sum_{n=0}^{N-n'-1} \hat{u}^*(n)\hat{u}(n+n'), \quad (8)$$

at lag $n' = 1$ and where * denotes the complex conjugation operator. For the above discussion, it has been assumed that the observation window consists of N lateral discrete samples ($n = 0, 1, ..., N - 1$), *i.e.*, the data kernel is taken parallel to the shear wave interference pattern axis. Finally, the 1-D mean shear velocity estimate $\langle v_s \rangle_{1D}$ for a 1-D data kernel is given as follows (Hoyt et al. 2006):

$$\langle v_s \rangle_{1D} = \frac{2\pi(2f_s + \Delta f_s)T_n}{\tan^{-1}\left\{\frac{\mathrm{Im}[\hat{\gamma}(1)]}{\mathrm{Re}[\hat{\gamma}(1)]}\right\}}, \quad (9)$$

which indicates that the local shear velocity can be estimated from spatial shear wave interference patterns (or crawling wave image frame) given knowledge of the source vibration frequencies and spatial sampling rate. Because eqn (9) produces a local shear velocity estimate, 2-D spatial distributions (for a given region-of-interest) are obtained by one-sample shifting the kernel throughout the shear wave displacement field. The resultant matrix is imaged and termed a shear velocity sonoelastogram.

Two-dimensional shear velocity estimation

Analogous to the approach introduced in the previous section, the shear velocity in 2-D space can be estimated by evaluating the phase of the 2-D autocorrelation function $\hat{\gamma}(m', n')$ of the analytic signal $\hat{u}(m, n)$:

$$\hat{\gamma}(m',n') = \sum_{m=0}^{M-m'-1}\sum_{n=0}^{N-n'-1} \hat{u}^*(m,n)\hat{u}(m+m', n+n'), \quad (10)$$

at lags ($m' = 1, n' = 0$) and ($m' = 0, n' = 1$). Equation (10) assumes that the observation window consists of M axial samples ($m' = 0, 1, ..., M - 1$) and N lateral samples ($n = 0, 1, ..., N - 1$). Lastly, the mean shear velocities $\langle v_s \rangle_m$ and $\langle v_s \rangle_n$ as estimated independently and relative to the m-axis and n-axis, respectively, are given by the following expressions:

$$\langle v_s \rangle_m = \left| \frac{2\pi(2f_s + \Delta f_s)T_m}{\tan^{-1}\left\{\frac{\mathrm{Im}[\hat{\gamma}(1,0)]}{\mathrm{Re}[\hat{\gamma}(1,0)]}\right\}} \right| \quad (11)$$

and

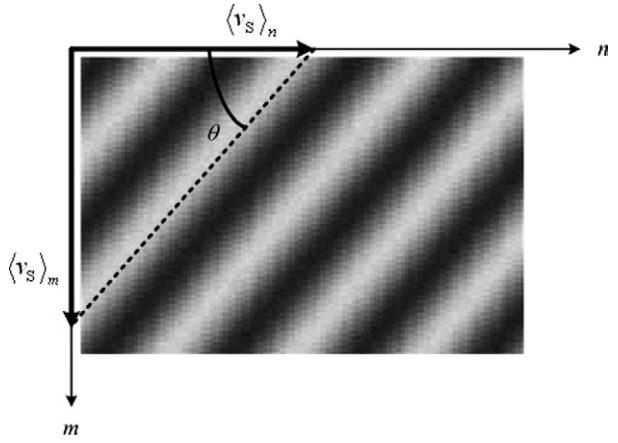

Fig. 1. Two-dimensional description of the mean shear velocity vectors in relation to a representative shear wave interference pattern. Note that local increases in shear wavelength (for a fixed vibration frequency) correspond to local increases in shear velocity values.

$$\langle v_s \rangle_n = \left| \frac{2\pi(2f_s + \Delta f_s)T_n}{\tan^{-1}\left\{ \frac{\mathrm{Im}\left[\hat{\gamma}(0,1)\right]}{\mathrm{Re}\left[\hat{\gamma}(0,1)\right]} \right\}} \right| \tag{12}$$

where T_m denotes the spatial sampling interval along the m-axis (*i.e.*, longitudinal direction).

Consideration of eqns (11) and (12) allows definition of an angular component θ (see Fig. 1):

$$\theta = \tan^{-1}\left(\frac{\langle v_s \rangle_m}{\langle v_s \rangle_n} \right). \tag{13}$$

Introduction of eqn (13) allows realization of a 2-D mean shear velocity estimate $\langle v_s \rangle_{2D}$ by projecting the 2-D shear velocity vector onto the n-axis:

$$\langle v_s \rangle_{2D} = \langle v_s \rangle_n \sin\theta. \tag{14}$$

Furthermore, by noting the following trigonometric relationship:

$$\tan^{-1}x = \sin^{-1}\left(\frac{x}{\sqrt{x^2+1}} \right), \tag{15}$$

combining eqns (13), (14) and (15) results in the following expression:

$$\langle v_s \rangle_{2D} = \frac{\langle v_s \rangle_m}{\sqrt{\left(\frac{\langle v_s \rangle_m}{\langle v_s \rangle_n} \right)^2 + 1}} \tag{16}$$

indicating that the 2-D local shear velocity can be estimated from the spatial shear wave interference patterns given knowledge of the source vibration frequencies and spatial sampling rate. In the derivation of eqn (16), we assume that, within the region defined by our kernel size, the tissue property is approximately homogeneous and the local shear wave interference patterns can be approximated as plane waves. Because eqn (16) produces a local shear velocity estimate, 2-D spatial distributions are obtained by one-sample shifting the kernel throughout the shear wave displacement field.

SIMULATIONS

Methods

To evaluate shear velocity estimation techniques, sonoelastographic simulation programs were implemented using MATLAB 7.0 (Mathworks, Inc., Natick, MA, USA). The first model assumes plane wave conditions and that the instantaneous shear wave interference patterns (*i.e.*, shear wave displacement vector) propagating in a locally homogeneous and isotropic medium can be described by eqn (5). The shear wave signal-to-noise ratio (SNR) was implemented by superimposing 25 dB of Gaussian noise onto the simulated shear wave displacement field. For all simulated data, the effects of shear wave reflection (for two-phase mediums) and attenuation have been omitted, *i.e.*, α is set to zero in eqn (5). Because shear velocity estimation algorithms require complex datasets, analytic images were produced from the real-valued shear wave displacement fields using a computationally efficient fast Fourier transform (FFT) method described by Marple (1999). Subsequently, local 1-D and 2-D shear velocity estimates were computed using eqns (9) and (16), respectively, with shear velocity sonoelastograms generated using techniques described previously in the *Theory* section.

Heterogeneous tissues can cause propagating shear waves to diffract and deviate from plane wave conditions. To assess shear velocity estimators exposed to these wave conditions, a crawling wave image (excited using a vibration frequency of 200 Hz) was simulated with 25 dB of additive Gaussian noise superimposed to mimic a spherically diverging interference pattern. Simulated crawling wave images were premised on eqn (5) but were implemented to allow for wavefront spreading. Specifically, these displacement images were generated by incrementally rotating the lateral displacement vector (described by eqn (5)) about the central image depth axis and throughout the image plane. Note that along these displacement vectors, the local shear velocity is 2 m/s and is equal to the product of the vibration frequency and twice the spatial wavelength. For this dataset, shear velocity estimates were calculated using the following configurations: 1-D data kernel and 1-D estimator described by eqn (9), 2-D data kernel and 1-D estimator described by eqn (12) and 2-D data kernel and 2-D estimator described by eqn (16). Default parameters for all simulations are listed in Table 1 unless otherwise stated.

Table 1. Default values used for simulation studies

Parameter	Value
Vibration source seperation (D)	40 mm
Vibration frequency (f_s)	200 Hz
Lateral spatial sampling interval (T_n)	0.4 mm
Axial spatial sampling interval (T_m)	0.15 mm
Quantization levels (Q_{LVL})	256
Signal-to-noise ratio (SNR)	25 dB

Results

Sonoelastographic crawling wave image frames (*i.e.*, shear wave interference patterns) were simulated representing perfect plane shear waves propagating through a two-phase medium separated by a sharp boundary (Fig. 2). The simulated shear velocities for this medium were 2 and 4 m/s, corresponding to relatively soft and hard materials, respectively. Note that because of the intrinsic properties of interfering shear waves, the spacing between pattern bands equals half of the shear wavelength. More specifically, the apparent wavelengths for this two-phase medium are 5 and 10 mm, respectively, given an excitation source frequency of 200 Hz and the shear velocities indicated.

Derived from the crawling wave image depicted in Fig. 2, shear velocity sonoelastograms illustrated in Fig. 3 were generated using the 1-D and 2-D processing techniques and spatial kernels of varying size. In the presence of noise, it is evident that the 2-D shear velocity estimator outperforms the 1-D–based estimation technique. It is important to note that because the simulated crawling wave images reflect plane wave conditions, the reduction in estimator variance using the 2-D sonoelastographic shear velocity estimation technique is the result of utilizing a 2-D kernel and not that of estimating the local shear velocity as a vector quantity. Because local shear velocity estimates correspond to the mean value within a given spatial kernel, extending the kernel dimension effectively decreases estimator variability by incorporating more shear wave information into the estimation process. However, as profile plots taken across the shear velocity sonoelastograms indicate, larger kernel sizes increase the transition zone between the two phases. As inferred from the profile plots in Fig. 3, the transition zone length is approximately equal to the size of the estimator kernel in that dimension. Thus, a fundamental tradeoff is introduced: increasing the kernel size to minimize estimator variance decreases the spatial resolution and increases transition zone length between the two contrasting mediums. Note that for the spatial sampling intervals used, transverse kernel sizes of 8, 12 and 16 samples corresponds to 3.2, 4.8 and 6.4 mm, respectively.

A simulated (noisy) crawling wave image with a spherically diverging wavefront and matched shear velocity sonoelastograms generated using 1-D and 2-D shear velocity estimation techniques are depicted in Fig. 4. Although the 1-D shear velocity estimation technique applied to either 1-D or 2-D data kernels fails to precisely describe the true underlying shear velocity throughout the image plane, the 2-D estimator produces a uniform and accurate shear velocity distribution. When processing nonplanar (or distorted waveform) crawling wave images, shear velocity sonoelastographic imaging using a 2-D estimator outperforms the 1-D–based techniques because of the vector-based computational approach. Using a 1-D kernel, the apparent local wavelength (in the lateral direction) may appear longer on a nonplanar shear wave field, resulting in an elevated local shear velocity estimate as shown in Fig. 4. Although using a 1-D estimator coupled with 2-D kernels yields a shear velocity distribution with lower levels of image noise (because of averaging over the axial kernel dimension), this approach still produces erroneous results. However, a 2-D kernel compounded with 2-D sonoelastographic shear velocity (vector) estimation allows for accurate description of the true shear velocity distribution.

EXPERIMENTS

Methods

Crawling wave datasets were collected from two homogeneous elasticity phantoms with differing shear moduli. The true shear velocities in these phantoms were determined using shear wave time-of-flight measurements. Shear velocity sonoelastograms were generated using the local 1-D and 2-D shear velocity estimation techniques described in the *Theory* section. From sequences of shear velocity sonoelastograms equating to

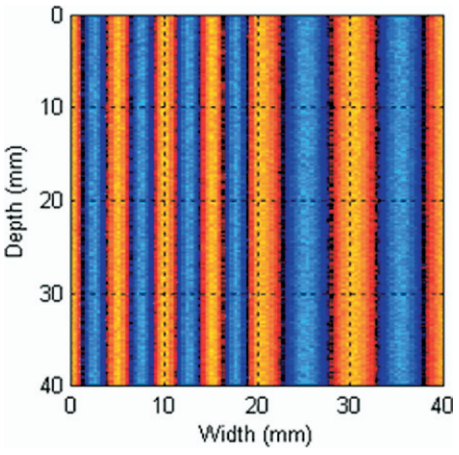

Fig. 2. Simulated crawling wave image excited using a shear wave vibration frequency of 200 Hz. Sonoelastogram corresponds to a two-phase medium with 25 dB of Gaussian noise superimposed. The shear velocities for this medium were 2 and 4 m/s, left and right of the 20-mm-width division, respectively.

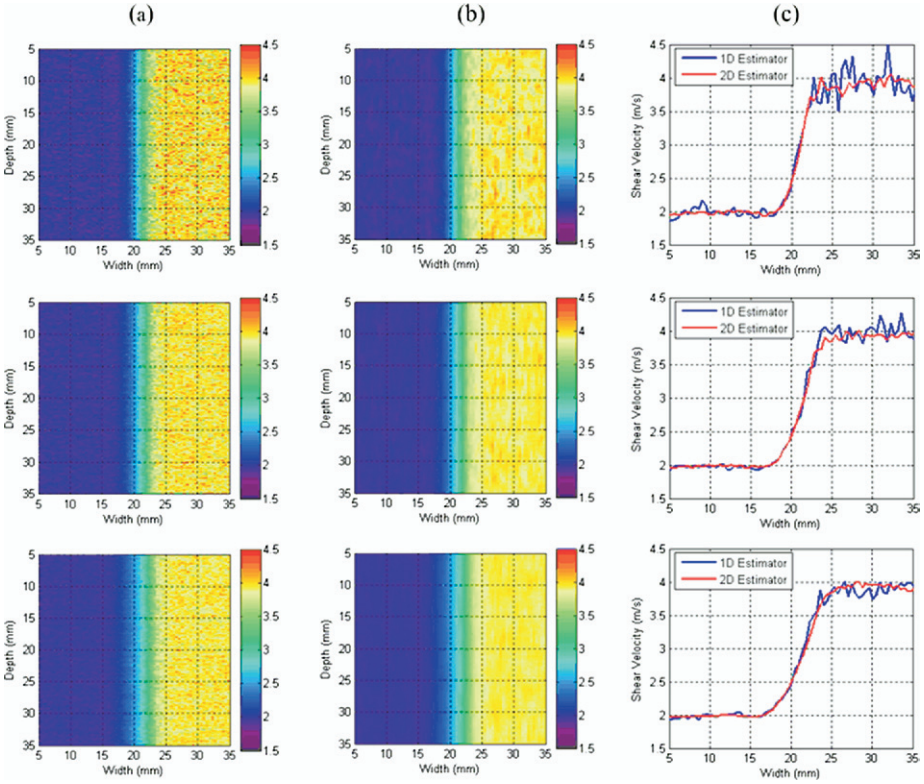

Fig. 3. Shear velocity sonoelastograms for a two-phase medium derived from a simulated crawling wave image. Shear velocity sonoelastograms (units of m/s) were produced using kernel sizes of (a) [1,8], [1,12] and [1,16] samples and (b) [8,8], [12,12] and [16,16] samples, top to bottom, respectively. Cross-sectional plot profiles taken at a depth of 20 mm are shown in (c) and indicate the transition zone length between the two regions.

one full cycle of shear wave motion (deduced from the underlying crawling wave sequence), shear velocity statistics were computed and compared with physical measurements (*i.e.*, ground truth values) for assessing estimator accuracy. A detailed description of the experimental setup used to collect the sonoelastographic data reintroduced in this paper can be found in Hoyt et al. (2006).

To assess lesion detection and contrast using shear velocity sonoelastographic imaging, heterogeneous elasticity phantoms were constructed using a two-step process. The first step involved production of stiff spherical inclusions and the second step entailed embedding these inclusions in otherwise soft homogeneous backgrounds. Regarding the inclusion fabrication protocol, a combination of 107.5 g/L of gelatin powder (300 Bloom Pork Gelatin, Gelatin Innovations Inc., Schiller Park, IL, USA), 0.75 g/L of graphite powder (Catalog No. G67-500, Fisher Scientific, Fair Lawn, NJ, USA) and 1.0 g/L of an antibacterial agent (Germall Plus, Chemical Marketing Concepts, New Milford, CT, USA) were mixed slowly into 0.5 L of distilled water. A homogeneous gel was produced by raising the temperature of the solution to 45° C in a constant temperature water bath (Hall et al. 1997). The mixture was then allowed to cool to 30° C (near the congealing point) before pouring into custom-made 5- and 10-mm spherical inclusion molds. Molds were subsequently stored in a cold room (5° C) for 24 hours to ensure that the gel inclusions congealed. Once congealed, each inclusion was threaded with a 0.125-mm-diameter pliable metal rod and suspended into the individual phantom containers (13 × 13 × 8 cm) at the desired depth. Subsequently, the background material for the heterogeneous phantoms was fabricated using the same protocol as described before, but using the following components: 50 g/L of gelatin powder, 0.75 g/L of graphite powder, 1 g/L of antibacterial agent and 2.0 L of distilled water. Once the background gel cooled to 30° C, the solution was poured into the phantom containers and placed in a cold room for 24 hours for congealing. Once solidified, the metal roads were removed from the phantom materials before scanning.

To demonstrate the potential for sonoelastographic shear velocity imaging in tissue, a fresh porcine liver was obtained after slaughter and stored in saline solution. Subsequently, a localized thermal lesion was created in the liver specimen using radiofrequency ablation (RFA) (Curley 2001). Specifically, an RF needle electrode

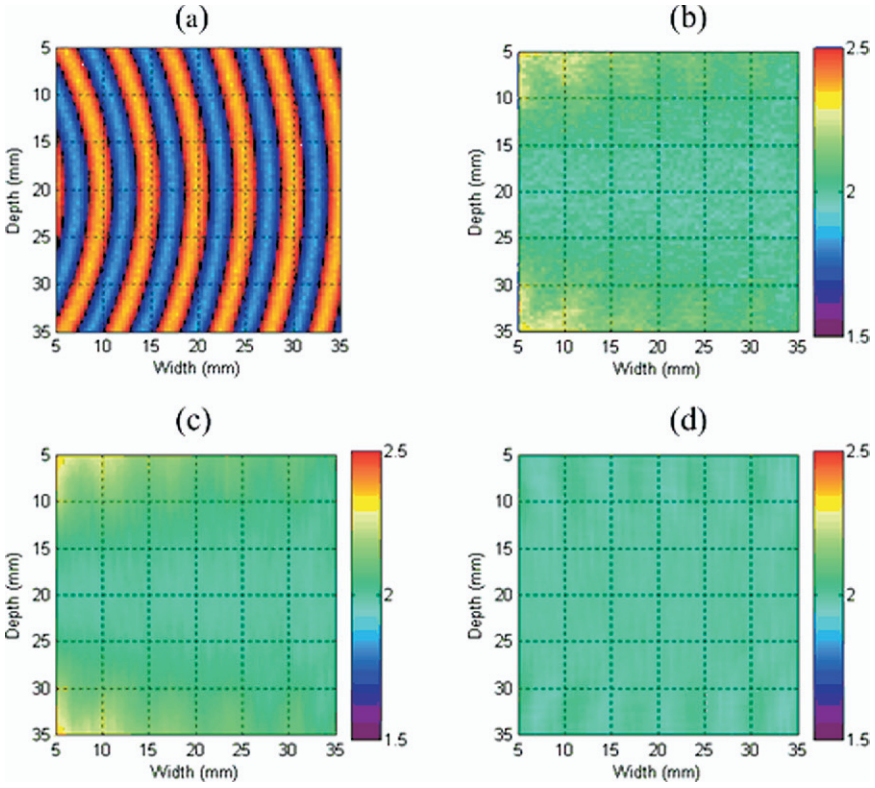

Fig. 4. (a) Simulated crawling wave image with a diverging wavefront and 25 dB of Gaussian noise superimposed excited using a shear wave vibration frequency of 200 Hz. Shear velocity sonoelastograms (units of m/s) were produced using the following configurations: (b) 1-D estimator applied to kernel sizes of [1,12] samples, (c) 1-D estimator applied to kernel sizes of [12,12] samples and (d) 2-D estimator applied to kernel sizes of [12,12] samples. The true shear velocity for this medium was 2 m/s.

(LeVeen Needle Electrode, Boston Scientific, Natick, MA, USA) was inserted into the liver specimen under ultrasound guidance to the desired location and then the hooked-shaped electrode arms (or tines) were deployed into the tissue. The needle electrode was then connected to an RF generator (RF 3000 Radiofrequency Ablation System, Boston Scientific) and grounding pads attached to the tissue specimen at a location remote to the ablation site. Application of RF energy induced coagulation necrosis and formation of a stiff lesion centered at the needle tip. After the RFA procedure, the liver specimen was embedded in a gelatin-based mold to facilitate sonoelastographic imaging. The tissue specimen was suspended in a gelatin mixture using the same protocol as described previously for inclusion phantom fabrication, but using the following components: 69 g/L of gelatin powder, 1.5 g/L of graphite powder, 9 g/L sodium chloride (Catalog No. VW6430-5, VWR International, West Chester, PA, USA) and 2.0 L of distilled water. After sonoelastographic imaging, gross pathology was obtained for the liver specimen and photographed. Finally, the RFA lesion was dissected and a fluid displacement technique was used to determine lesion volume.

Two vibration sources (Model 2706, Brüel & Kjaer, Naerum, Denmark) were fitted with surface-abraded extensions having an effective contact region of 80 × 10 mm. These extensions were placed in contact with opposing lateral boundaries of the respective scanning materials with the long axis (and induced shear vibration) parallel to, and in line with, the desired image plane (governed by transducer positioning). A two-channel signal generator (Model AFG320, Tektronix, Beaverton, OR, USA) produced two monochrome low-frequency signals that were passed through power amplifiers (Model 2706, Brüel & Kjaer) before being input to the vibration sources. Phase shifting one of the vibration excitation signals allowed spatial translation of shear wave interference patterns across the image plane. This approach is analogous to implementing a frequency offset between the two excitation signals but establishes a pseudo-triggering functionality for controlling shear wave interference motion and data acquisition.

For all experiments, a LOGIQ 9 ultrasound scanner (General Electric Medical Systems, Milwaukee, WI, USA) modified for sonoelastographic imaging was used with a M12L linear array probe (5–13 MHz bandwidth)

for real-time visualization of crawling wave sonoelastograms. The frame rate for the sonoelastographic system is typically greater than 12 frames per second and dependent on the user-defined scanning field-of-view. This unit allows access to the unprocessed demodulated datasets (*i.e.*, in-phase and quadrature signals) that were stored and transferred to an external computer for processing shear velocity sonoelastograms. For the embedded liver specimen, scanning was performed using a 3-D protocol. Using this approach, crawling wave sonoelastograms were obtained at 1.0-mm spacing by mounting the probe on a motorized track (Velmex, Bloomfield, NY, USA). Complete lesion coverage permits volume reconstructions from the 2-D shear velocity sonoelastograms.

Sonoelastographic shear velocity imaging was further assessed in both the inclusion phantoms and embedded tissue specimen using the experimental setups described previously. Sequences of eight crawling wave sonoelastograms were obtained (or one full cycle of shear wave motion), and matched shear velocity images were generated and averaged. For all results presented, spatial filtering of crawling wave images was performed before shear velocity sonoelastogram processing. Derived from the inclusion phantom-based images, the sonoelastogram contrast-to-noise ratio (CNR) was quantified as follows:

$$\mathrm{CNR} = \frac{\mu_I - \mu_B}{\sigma_B} \tag{17}$$

where μ and σ denote mean and standard deviation of shear velocity estimates, respectively, and the subscripts I and B indicate homogenous image regions of the inclusion and background, respectively. The computed contrast values were obtained from rectangular phantom regions as illustrated in Fig. 5. For liver tissue experiments, a 3-D lesion (*i.e.*, volume) was segmented using a semiautomatic technique (Castaneda et al. 2007) from the series of shear velocity sonoelastograms.

Results

The results shown in Fig. 6 illustrate representative crawling wave and shear velocity sonoelastograms (processed using both 1-D and 2-D shear velocity estimation techniques) for the relatively soft and hard homogeneous elasticity phantoms. For a given vibration frequency, crawling wave sonoelastograms from the softer elasticity phantom exhibit higher spatial frequencies than that observed from the harder elasticity phantom, thus indicating a lower true shear velocity distribution as supported by the shear velocity imaging results. Shear velocity statistics were computed from these imaging results and compared with measured true shear velocities (Fig. 7).

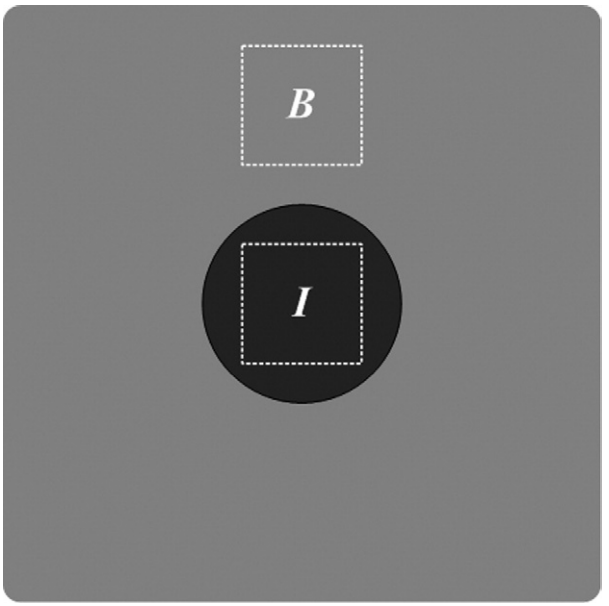

Fig. 5. Illustration of a typical inclusion phantom-based sonoelastogram and corresponding background (*B*) and inclusion (*I*) regions selected for analysis of the image contrast-to-noise ratio (CNR).

As these plots summarize, shear velocity sonoelastograms describe accurately the true shear velocity distributions across a broad range of vibration frequencies. Because the gelatin-based phantoms exhibit elastic behavior (*i.e.*, no viscous effects), shear velocity estimates are independent of the applied shear wave frequency and governed by eqn (4). However, for the harder elasticity phantom vibrated at lower frequencies (<250 Hz), imaging results overestimate the true shear velocity measurements. This degradation in accuracy is attributed to spatial shear wavelengths being considerably larger than the estimator kernel size. In general, 1-D and 2-D sonoelastographic shear velocity imaging techniques yield comparable results in homogeneous phantoms (for a given kernel size), with the latter exhibiting lower levels of estimator noise.

Experimental sonoelastographic results were obtained from heterogeneous elasticity phantoms containing either a 5- or 10-mm stiff isoechoic spherical inclusion (Fig. 8). Shear wave propagation was induced using a vibration frequency of 200 Hz and, subsequently, shear velocity sonoelastograms were processed using spatial kernels of varying size and using the 1-D and 2-D shear velocity estimation techniques (Figs. 9 and 10, respectively). Inspection of Fig. 8 shows that shear wave interference patterns exhibit decreases in spatial frequency local to the inclusion, owing to an elevated shear velocity. As results demonstrate, employing larger kernel sizes produces shear velocity sonoelastograms with lower lev-

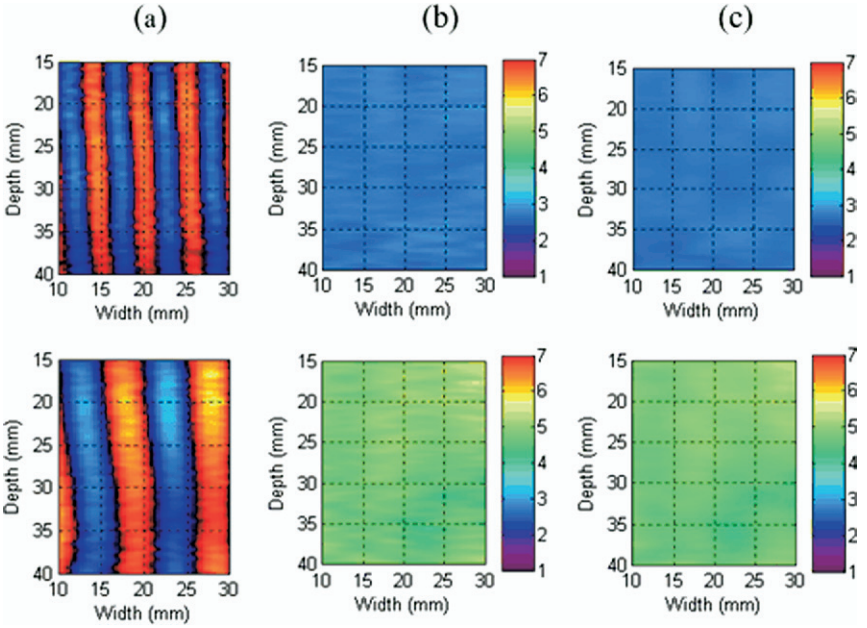

Fig. 6. Experimental sonoelastographic results from relatively soft (top) and hard (bottom) homogeneous phantoms. Depicted are (a) shear wave interference patterns excited using a vibration frequency of 250 Hz and shear velocity sonoelastograms (units of m/s) produced using kernel sizes of (b) [1,12] and (c) [12,12] samples.

els of image noise. Specifically, the corresponding CNR values for the sonoelastograms depicted in Figs. 9 and 10 are listed in Table 2, which reveals that the 2-D sonoelastographic shear velocity estimation technique outperforms the 1-D version for a given kernel size in terms of image noise minimization and contrast enhancement. However, because local shear velocity values are the

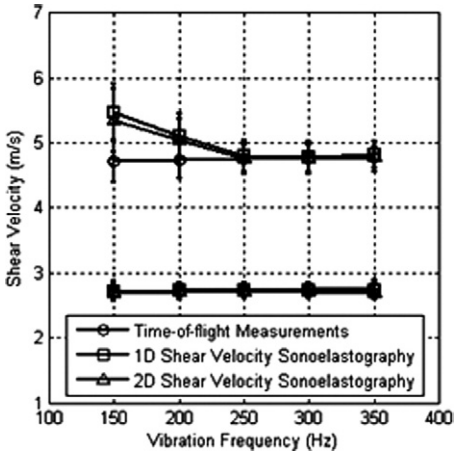

Fig. 7. Matched shear velocities as estimated from sequences of shear wave interference sonoelastograms and sets of physical measurements (*i.e.*, shear wave time-of-flight). Statistical results were acquired as a function of shear wave vibration frequency and from the relatively soft (bottom set of plots) and hard (top set of plots) homogeneous phantoms.

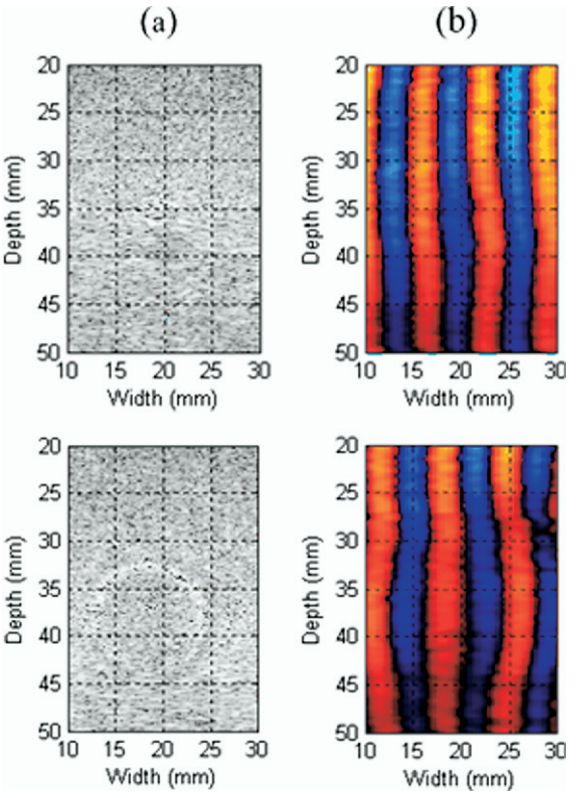

Fig. 8. Matched (a) B-mode ultrasound and (b) shear wave interference pattern images from heterogeneous phantoms with a 5-mm (top) or 10-mm (bottom) stiff cylindrical inclusion excited using a shear wave vibration frequency of 200 Hz.

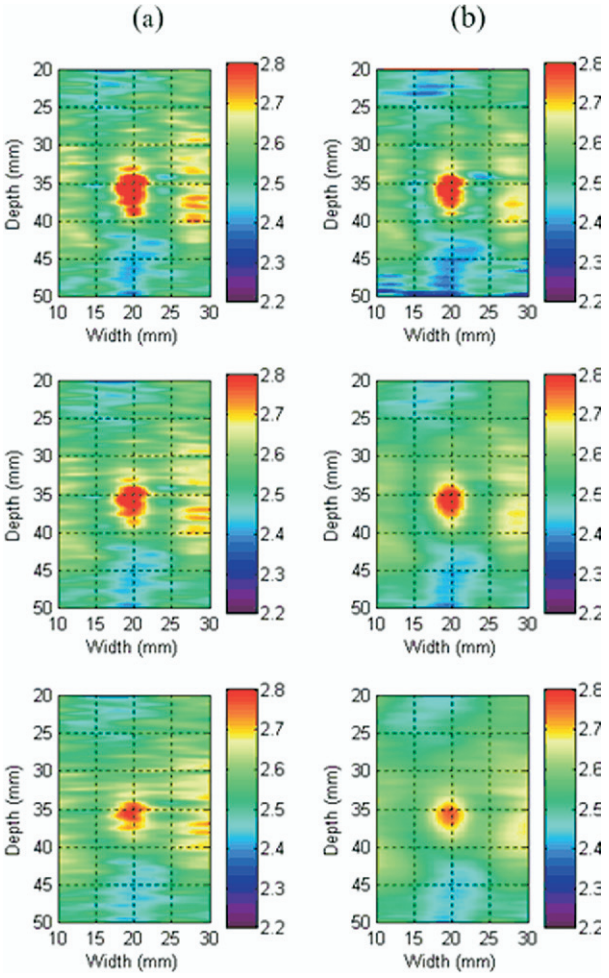

Fig. 9. Experimental shear velocity sonoelastographic results from a heterogeneous phantom with a 5-mm stiff cylindrical inclusion excited using a shear wave vibration frequency of 200 Hz. Shear velocity sonoelastograms (units of m/s) were produced using kernel sizes of (a) [1,8], [1,12] and [1,16] samples and (b) [8,8], [12,12] and [16,16] samples, top to bottom, respectively.

mean value estimates for a given kernel of shear wave displacement data, utilizing kernel sizes comparable to lesion size implies that a majority of spatial information may be obtained from the softer background material and, thus, lead to an underestimation of the true shear velocity in the stiffer inclusion (and *vice versa* for a relatively softer inclusion). In addition, comparing 1-D and 2-D–based shear velocity sonoelastograms in Figs. 9 and 10, respectively, reveals lateral streak artifacts in the former, which are attributed to the 1-D nature of the estimation process and the failure to incorporate crawling wave information from neighboring depth locations. Cross-sectional profile plots depicted in Fig. 11 further indicate that larger kernel sizes produce larger transition zone lengths about the background/inclusion boundary, with the overall transition zone length approximately equal to the size of the estimator kernel. Therefore, a fundamental tradeoff exists between transition zone length and shear velocity estimator kernel size.

Experimental sonoelastographic results from an embedded porcine liver specimen with RFA-induced lesion are shown in Fig. 12. Shear wave interference patterns were excited using a vibration frequency of 60 Hz, and shear velocity sonoelastograms were processed using both the 1-D and 2-D estimation techniques. Although no discernible lesion is evident in the B-mode ultrasound image, shear velocity sonoelastograms reveal a focal lesion in the image plane characterized by an elevated shear velocity distribution. Specifically, shear velocity estimates were approximately 2.2 and 3.0 m/s for the

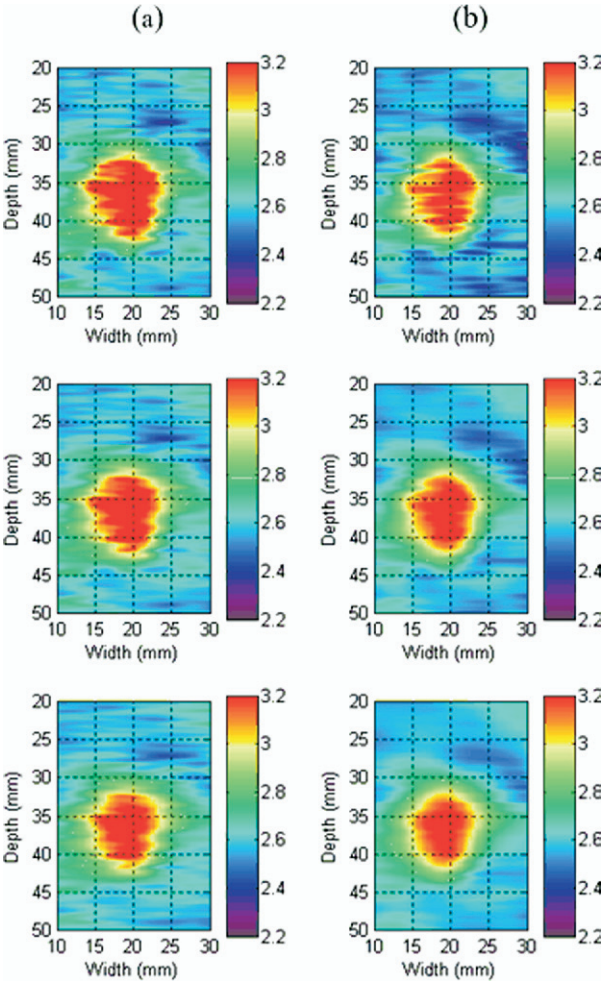

Fig. 10. Experimental shear velocity sonoelastographic results from a heterogeneous phantom with a 10-mm stiff cylindrical inclusion excited using a shear wave vibration frequency of 200 Hz. Shear velocity sonoelastograms (units of m/s) were produced using kernel sizes of (a) [1,8], [1,12] and [1,16] samples and (b) [8,8], [12,12] and [16,16] samples, top to bottom, respectively.

Table 2. Summary of contrast-to-noise ratios (CNR) from sonoelastograms of 5-mm and 10-mm tissue-mimicking inclusion phantoms

Contrast-to-noise ratio (CNR)		
Kernel size [M,N]	5-mm inclusion phantom	10-mm inclusion phantom
[1,8]	9.0	30.7
[1,12]	8.6	33.1
[1,16]	7.9	34.3
[8,8]	13.3	40.5
[12,12]	14.8	48.3
[16,16]	21.5	62.7

Sonoelastograms were processed using both the 1-D and 2-D shear velocity sonoelastographic estimation techniques and kernels of varying size (samples).

normal liver and RFA lesion, respectively, which is in agreement with those values presented by Taylor et al. (2001). Furthermore, inspection of 1-D and 2-D–based shear velocity sonoelastograms reveals less image noise artifacts and a more consistent lesion boundary for the latter when compared with the gross pathology photograph (albeit with possible misregistration between image planes), which is a significant property for any potential clinical application. Volume measurements of the RFA lesion obtained from shear velocity sonoelastograms (1.7 cm^3) was comparable to that obtained by fluid displacement of the dissected lesion (2.2 cm^3) as illustrated by the 3-D (volume) reconstructions in Fig. 13. It is important to mention that liver tissue is known to exhibit viscoelastic properties and shear velocity (or modulus) measurements will be frequency dependent (Kruse et al. 2000). However, acquiring an ensemble of shear velocity sonoelastograms for a range of shear wave excitation frequencies may permit a more accurate description of tissue properties given appropriate selection of a viscoelastic model. Notwithstanding, sonoelastographic shear velocity results presented in Figs. 12 and 13 demonstrate feasibility of this imaging technique in tissue and warrants further investigation.

CONCLUSIONS

In this paper, a novel 2-D sonoelastographic technique for estimating local shear velocities from propagating shear wave interference patterns (termed crawling waves) is introduced. A relationship between the local

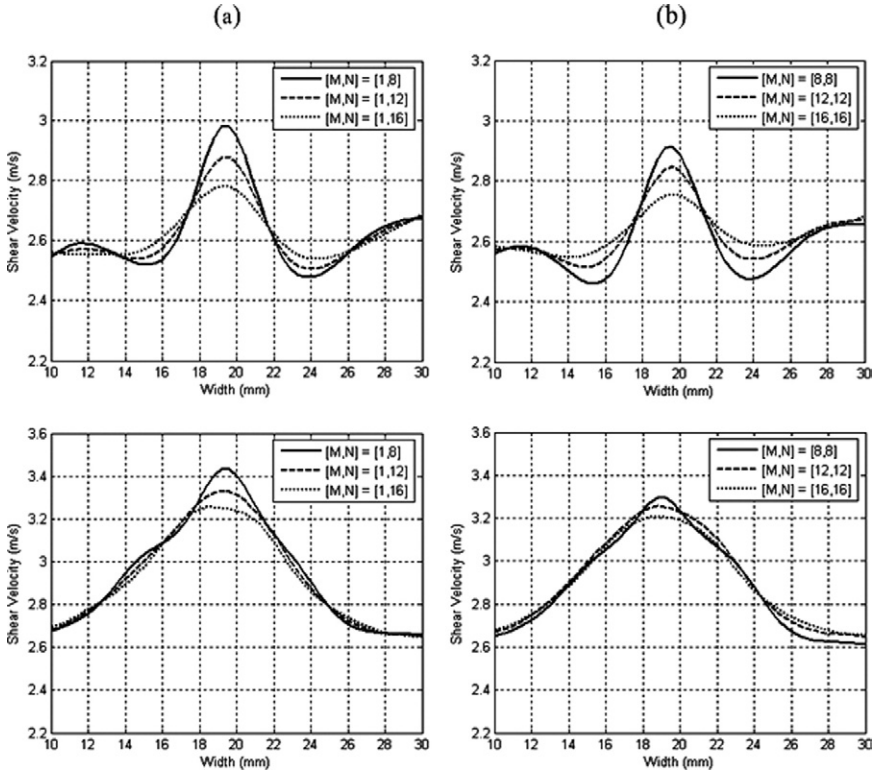

Fig. 11. Cross-sectional plot profiles derived from the (a) 1-D and (b) 2-D shear velocity sonoelastograms depicted in Figs. 9 and 10, top and bottom, respectively, and taken at a depth of approximately 36 mm. Results illustrate the transition zone length and image contrast, as a function of estimator kernel size, between the soft background material stiff inclusions.

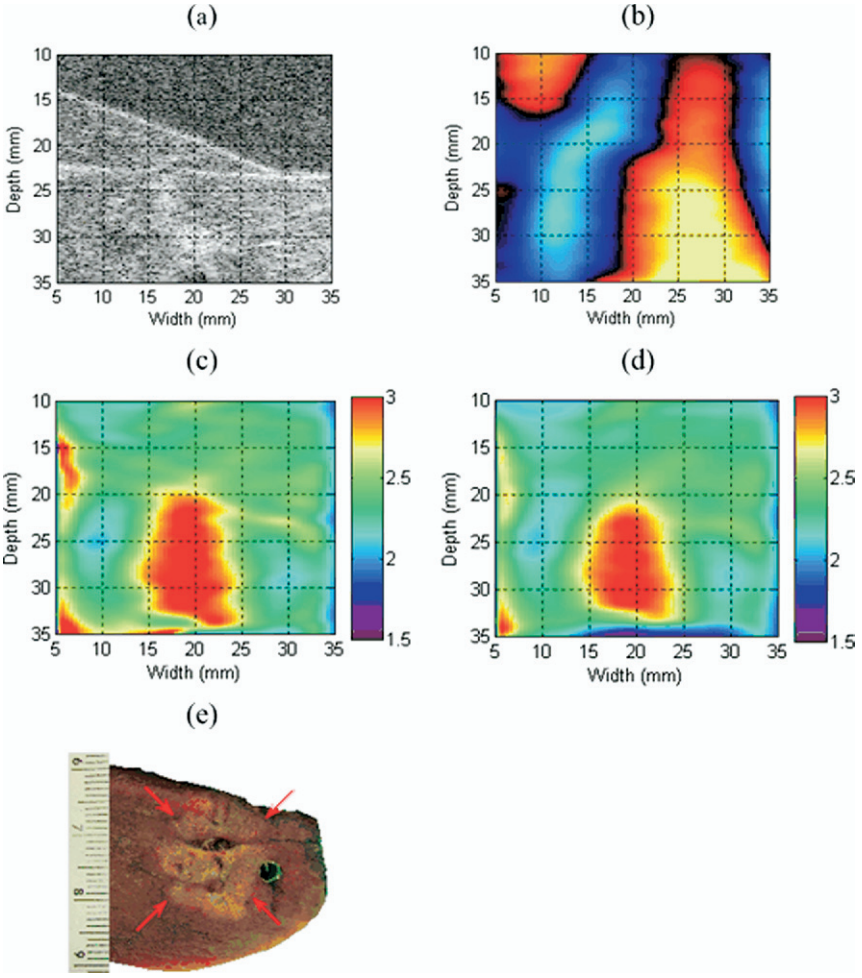

Fig. 12. Experimental sonoelastographic results from porcine liver specimen with RFA-induced lesion. Tissue specimen was embedded in a gelatin block and shear wave interference patterns were excited using a vibration frequency of 60 Hz. Results depict (a) B-mode ultrasound image, (b) shear wave interference patterns, shear velocity sonoelastograms (units of m/s) produced using kernel sizes of (c) [1,16] samples and (d) [16,16] samples and (e) gross pathology photograph with lesion demarcated by arrows (bottom left).

crawling wave spatial phase derivatives and local shear wave velocity is derived with phase derivatives estimated using a 2-D autocorrelation technique. Comparisons were made between the 2-D sonoelastographic shear velocity estimation technique and its computationally simpler 1-D precursor.

In general, 2-D sonoelastographic shear velocity estimation outperformed the 1-D–based technique in terms of minimizing shear velocity estimate noise and image artifacts. For both approaches, increasing the estimator kernel size reduces noise levels but lowers spatial resolution. Moreover, the 2-D sonoelastographic shear velocity technique was shown in simulation to accurately reconstruct the true shear velocity distribution from a noisy spherically diverging field, whereas the 1-D estimator failed. Results from homogeneous elastic phantoms demonstrate experimentally the ability of sonoelastographic shear velocity imaging to quantify the true underlying shear velocity distributions as verified using time-of-flight measurements. From heterogeneous elastic phantom results, sonoelastogram CNR values reveal that the 2-D sonoelastographic shear velocity estimation technique outperforms the 1-D version for a given kernel size in terms of image noise minimization and contrast enhancement. Furthermore, results also indicate that increasing the estimator kernel size increases the transition zone length about boundaries in heterogeneous elastic mediums and may complicate accurate quantification of smaller elastically contrasting lesions. Experimental sonoelastographic shear velocity imaging results from an embedded porcine liver specimen with a RFA-induced lesion were presented demonstrating potential for quantitative imaging and lesion volume determination in tissue. Comparison of 1-D and 2-D sonoelastographic shear

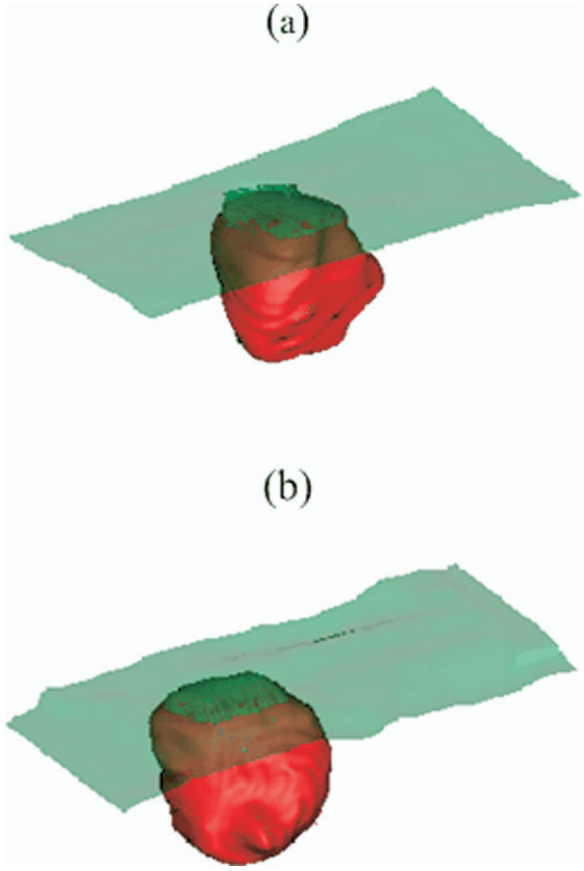

Fig. 13. Three-dimensional reconstructions of an RFA lesion (red) in liver from segmented (a) shear velocity sonoelastograms and (b) gross pathology photographs. Segmentation of liver tissue boundary (green) for shear velocity sonoelastographic results was obtained from the coregistered B-mode ultrasound images. Lesion volumes obtained from imaging (1.7 cm^3) are comparable to gross pathology (2.2 cm^3) results.

velocity results from the tissue specimen reveals less image noise artifacts and a more consistent lesion boundary for the latter when compared with gross pathology. Overall, 2-D sonoelastographic shear velocity imaging from crawling waves is shown to be a promising new approach to characterizing the mechanical properties of elastic materials.

Acknowledgements—We are grateful for helpful suggestions from Drs. Deborah J. Rubens, John Strang, Zhe Wu and Man Zhang, and for the loan of equipment and expertise from General Electric (GE) Medical Systems. This work was supported by NIH Grant 5 R01 AG16317-05.

REFERENCES

Anderson WAD, Kissane JM. Pathology: Volume 2. St. Louis, MO: C.V. Mosby Co., 1977.

Castaneda B, Zhang M, Bylund K, Christensen J, Saad W, Rubens DJ, Parker KJ. Semiautomatic measurement of thermally ablated lesions in sonoelastographic images. J Ultrasound Med 2007;26:S87–S88.

Curley SA. Radiofrequency ablation of malignant liver tumors. Oncologist 2001;6:14–23.

Kruse SA, Smith JA, Lawrence AJ, Dresner MA, Manduca A, Greenleaf JF, Ehman AL. Tissue characterization using magnetic resonance elastography: Preliminary results. Phys Med Biol 2000;45: 1579–1590.

Landau LD, Lifshitz EM. Theory of elasticity. New York: Elsevier Butterworth-Heinemann, 1986.

Lerner RM, Parker KJ, Holen J, Gramiak R, Waag RC. Sonoelasticity: Medical elasticity images derived from ultrasound signals in mechanically vibrated targets. Acoust Imaging 1988;16:317–327.

Gao L, Parker KJ, Lerner RM, Levinson SF. Imaging of the elastic properties of tissue—A review. Ultrasound Med Biol 1996;22: 959–977.

Greenleaf J, Fatemi M, Insana M. Selected methods for imaging elastic properties of biological tissues. Annu Rev Biomed Eng 2003;5:57–78.

Hall TJ, Bilgen M, Insana MF, Krouskop TA. Phantom materials for elastography. IEEE Trans Ultrason Ferroelectr Freq Control 1997; 44:1355–1365.

Hoyt K, Parker KJ, Rubens DJ. Sonoelastographic shear velocity imaging: Experiments on tissue phantom and prostate. IEEE Ultrasonics Sympos 2006;1686–1689.

Huang SR, Lerner RM, Parker KJ. On estimating the amplitude of harmonic vibration from the Doppler spectrum of reflected signals. J Acoust Soc Am 1990;88:310–317.

Marple SL. Computing the discrete-time analytic signal via FFT. IEEE Trans Sign Proc 1999;47:2600–2603.

McLaughlin J, Renzi D, Parker KJ, Wu Z. Shear wave speed recovery using moving interference patterns obtained in sonoelastography experiments. J Acoust Soc Am 2007;121:2438–2446.

Ophir J, Alam SK, Garra B, Kallel F, Konofagou E, Krouskop T, Varghese T. Elastography: Ultrasonic estimation and imaging of the elastic properties of tissues. Proc Instr Mech Engrs 1999;213: 203–233.

Parker KJ, Fu D, Gracewski SM, Yeung F, Levinson SF. Vibration sonoelastography and the detectability of lesions. Ultrasound Med Biol 1998;24:1937–1947.

Taylor LS, Porter BC, Rubens DJ, Parker KJ. Three-dimensional sonoelastography: Principles and practices. Phys Med Biol 2000; 45:1477–1494.

Taylor LS, Richards MS, Moskowitz AJ, Lerner AL, Rubens DJ, Parker KJ. Viscoelastic effects in sonoelastography: Impact on tumor detectability. IEEE Ultrasonics Sympos 2001;1639–1642.

Wu Z, Taylor LS, Rubens DJ, Parker KJ. Sonoelastographic imaging of interference patterns for estimation of the shear velocity of homogeneous biomaterials. Phys Med Biol 2004;49:911–922.

Wu Z, Hoyt K, Rubens DJ, Parker KJ. Sonoelastographic imaging of interference patterns for estimation of shear velocity distribution in biomaterials. J Acoust Soc Am 2006;120:535–545.